

Inflow And Load Identification Of A Coupled Flap-Lag-Torsion Rotor Blade†

Jerry P. Higman††
Kawada Industries, Inc.
Tokyo, Japan

Liu ShouShen††
Nanjing University of Aeronautics and Astronautics
Nanjing, China

Daniel P. Schrage
Georgia Institute of Technology
Atlanta, Georgia, USA

Abstract

In this paper, a coupled flap-lag-torsion rotor blade load and inflow identification methodology has been developed and presented. This method determines the structural loads, displacements, airloads and inflow of a fully coupled flap-lag-torsion elastic rotor blade using measured blade response data. Specifically, the authors developed an "Inverse Transfer Matrix Method" for identifying coupled flap-lag rotor blade loads. Now, this method is extended to determine the coupled flap-lag-torsion rotor blade loads and the rotor inflow for the first time using the force analysis method. Blade load identification includes the blade structural model, the load identification process and the blade equations of motion which are based on a force analysis. The inflow identification approach, based on lifting-line theory and unsteady thin airfoil theory, is for the first time, developed and presented in this paper. The methods and processes are verified using simulated flapwise, chordwise and torsion moments and other response data that have been calculated using flight test airloads data. These flight test data were obtained from the NASA/Army UH-60A Black Hawk Airloads Program (BHAP). An error analysis is also performed to investigate the sensitivity of the identified parameters to random errors of measured data. The numerical results, including comparison with flight test data, show that the developed methods and processes are successful.

Notation

C_d, C_ℓ, C_m two-dimensional blade section coefficients

e_o distance at root between elastic axis and axis about which blade is rotating, positive when elastic axis lies ahead

EI_η, EI_ζ bending stiffness about the principal axes η and ζ , respectively

† This paper is based on portions of Dr. Higman's Ph.D. Thesis.

†† This work was completed while the authors were at the Georgia Institute of Technology.

Presented at the Twenty Second European Rotorcraft Forum, Brighton, England, September 16-19, 1996.

F_η, F_ζ, M_a external loadings in the η and ζ directions and about the x axis, respectively

GJ torsional rigidity

I_θ torsional mass moment of inertia

k_A^2 polar radius of gyration

k_ϕ control system stiffness

L_{yc} circulatory airload in the y direction of the airfoil coordinate system

L_{zc}, L_{znc} circulatory and noncirculatory airloads in the z direction of the airfoil coordinate system

M_{ac}, M_{anc} circulatory and noncirculatory aerodynamic moments

M_x, M_η, M_ζ bending moments about the elastic, major and minor principal axes, x, η and ζ , respectively

r distance of blade element mass from the center of rotation

S_η, S_ζ shear forces in the direction of the major and minor principal axes, η and ζ , respectively

v, w displacements of the elastic axis in the direction of the major and minor principal axes

X, Y, Z stationary shaft coordinate system or rotating hub coordinate system

x, y, z rotating blade coordinate system

η, ζ direction of the major and minor principal axes, respectively

$\Delta\theta$ built-in twist angle of the blade segment

$\Delta\phi$ change in torsional displacement along blade segment, ℓ

θ pitch angle of the blade section, positive when leading edge is up

ϕ torsional displacement about x axis, positive when leading edge is up

subscripts and superscripts

n nth blade station or element

$(\)''$ $d^2(\)/dt^2$

$(\)'$ $d(\)/dr$

$(\)_{\bar{\quad}}$ parameters at the left end of the massless elastic field and are in the principal axes coordinate system

$(\)_{\hat{\quad}}$ parameters due to coupling between bending and torsion associated with centrifugal forces

$(\)_{\tilde{\quad}}$ parameters at the right end of the massless elastic field and relate the moments across the mass

Introduction

A rotor blade, when undergoing flap, lag and pitch oscillations, experiences large variations in the aerodynamic loads along the blade span and during its rotation around the rotor's azimuth. The aerodynamic blade loads are highly motion dependent and, among other parameters, depend upon the coupled blade dynamic response and the unsteadiness of the air flow. These loads dictate the noise produced by the rotor due to stall and compressibility effects as well as blade vibration in conjunction with the inertial forces. Furthermore, they have a direct impact on the corresponding hub shears and fuselage vibration and overall power requirements of the helicopter. For these compelling reasons, to understand and accurately determine rotor airloads has long been a desire and worthy goal of the rotorcraft engineer to bring about a successful rotor design.

Two general directions have been taken to determine the motion-dependent blade loads. They are: 1) rotor load prediction and 2) rotor load identification. In the prediction method, noted as the "direct" problem, the airloads are "known" and the blade response is unknown. Conversely, in the identification method or "inverse" problem, the blade response is known and the airloads are unknown. Until recently, however, the limited amount and type of available flight test data has precluded the use of identification methods in a detailed rotor load study. In recent years, rotorcraft flight tests and wind tunnel tests have begun to use a larger quantity and greater variety of sensors to obtain more diverse and detailed measurements. Also in these tests, a greater number of flight conditions are being considered. As a result, rotor load identification has been gaining interest as a means to examine the dynamic nature of rotor blade response and loads. The identification methodology, in essence, is an approach to determine rotor loads from measured structural response data, such as measured strains at specific radial stations on the blade, local accelerations, and/or blade angles at the root measured on the blade during testing. This method is the "inverse" problem.

From the identified shear loads, the airloads and inflow acting on the blade can then be determined.

With this in mind, the objective of this study is to determine, through identification, the airloads and inflow of a fully coupled flap-lag-torsion rotor blade model.

Two standard methods for the identification of rotor blade loads have been considered by researchers thus far. The modal analysis method and the force analysis method, respectively. In the modal analysis method, the modal moments are used in conjunction with experimental bending and torsion moment data, to identify the set of coupled generalized coordinates. With the generalized coordinates identified, the blade deflections, slopes and shears are identified and the airloads are determined. In the second approach, the force analysis method uses bending and torsional moments obtained from experimental data in conjunction with an equilibrium analysis of the aerodynamic, inertial and structural bending-torsion moments to obtain the blade airloads. Each of the two methods have potential sources of errors. The modal deflection method is subject to the ill-condition problem requiring considerable engineering judgment and even the flap only case can be difficult to analyze. Also, this method uses only a finite set of dynamic modes which may not capture or represent certain physical phenomena of the problem. The force analysis method obtains the airloads from the difference between the inertial and shear loads. Since these loads nearly cancel on a rotor blade, the airloads calculation is sensitive to small errors in the inertial and shear loads calculations. References [1 and 2] considered the coupled flap-lag and torsion cases, respectively, for the blade load identification process. Because of the systematic approach employed in the force analysis method, the fact that it is not subject to

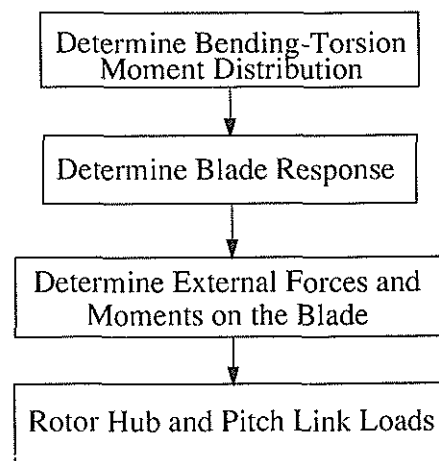


Fig. 1. Rotor Blade Load Identification Process

the ill-condition problem, and that it is readily applicable to the coupled blade bending-torsion case, the force analysis method was used in this study. The process for the force analysis method is shown in Fig. 1.

Blade Load Identification Model

The nonlinear equations of motion for the structural dynamics model of the rotor blade used in this analysis is based on the linear model formulated by Houbolt and

Brooks [3]. In Ref. [3], the set of partial differential equations of motion of the continuous system were developed to model an elastically coupled flap-lag-torsion rotor blade having twist and nonuniform structural properties. The rotating blade was assumed to be a slender, straight rotating beam with homogenous, isotropic properties. The blade cross section is assumed to be symmetric. The model, developed using the Newtonian approach of force and moment summation, accommodates mass centroid and area centroid axes offsets from the elastic axis. Also incorporated into the model are the provisions for a torque offset, variable pretwist and nonuniform mass and stiffness section properties. Blade structural damping, precone, sweep and droop, however, are not included.

The governing differential equations of motion for a rotating blade, formulated by Houbolt and Brooks, were adapted by Isakson and Eisley [4] to a matrix formulation using discretization. The equations for the continuous system were reposed as a set of finite difference equations using a lumped parameter methodology to obtain a solution for the set of differential equations of motion. The lumped parameter technique utilized in their work is a step-by-step or transfer matrix method. The transfer matrix method type of analysis was first posed by Holzer [5] in an analysis for the torsional vibration of shafts and later by Myklestad to analyze the flexural vibrations of beams [6]. The present analysis adapts this set of discretized rotor blade equations of motion for the basis of development of an inverse transfer matrix method to identify the airloads and inflow on the rotor blade for hover and forward flight. The equations are reformulated and extended to adapt them to the blade load identification approach. In this approach, the equations are formulated to employ coupled rotor blade bending and torsion moments, obtained from experimental strain measure data. In addition, depending on the type of rotor hub, blade root angles may be required.

In the development of the model rotor blade for load identification, the proper selection of the coordinate system for the governing equations needs to be considered. Specifically, the coordinate system used in this analysis should be compatible with the experimental data. Since blade strain gages are placed on the load bearing spar of the rotor blade to measure bending and torsion moments during wind tunnel or flight tests, it is necessary to choose the blade cross section coordinate axes or principal axes as the coordinate system. As such, the blade coordinate system is defined as the η coordinate parallel to the major axis, the ζ coordinate parallel to the minor axis of the cross section and the x coordinate completing the triad. The origin of η and ζ coordinates is taken at the elastic axis which is assumed to be a straight line for the undeformed blade. The section coordinates, displacements v , w , ϕ , bending and torsion moments M_η , M_ζ , M_x , shears S_ζ , S_η , and airloads F_ζ , F_η , M_a for the flapwise, chordwise and torsion directions are shown in Fig. 2. The blade response takes place within the rotating blade coordinate system x , y , z which has a translation, e_0 , from the rotating hub axes X_h , Y_h , Z_h to the blade axis to incorporate a torque offset shown in Fig. 3. The torque offset is positive as shown. The hub axis rotates about the stationary shaft axes X_s , Y_s ,

in the counter-clockwise direction when viewed from above. The velocity of the shaft axes system relative to the inertial reference frame is considered through the advance ratio and the shaft tilt.

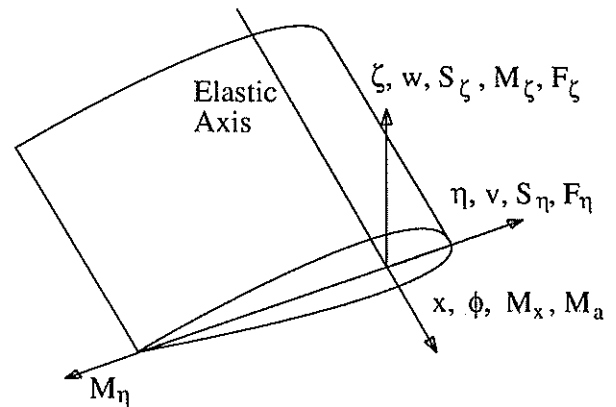


Fig. 2. Nomenclature for Cross-Section Coordinates, Displacements, Moments, Shears and Airloads

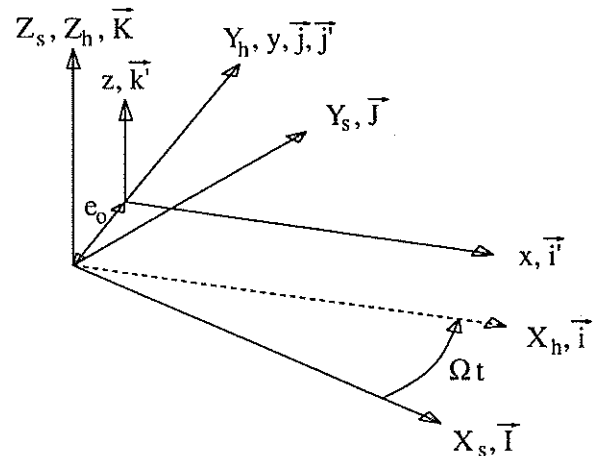


Fig. 3. Stationary Rotor Hub and Rotating Blade Coordinate Systems

The blade is divided into a number of spanwise elements, not necessarily equal in length, each of which consists of a massless elastic beam segment or field and a concentrated point mass or station. The flapwise bending stiffness EI_η , the chordwise bending stiffness EI_ζ and the torsional stiffness GJ are assumed constant between masses. Figure 4. shows the relationship between the elastic axis and the structural offset parameters where both the tensile and the mass centroids are defined as positive ahead of the elastic axis. The mass centroid and tensile axes, both of which are offset from the elastic axis, are defined at each blade segment.

The states S_ζ , M_η , w' , w , S_η , M_ζ , v' , v , M_x , ϕ , which are located at the right side of the mass station, are defined and represented along the blade at each of the spanwise segments and change in such a manner that the variation can be considered to occur in a series of steps. These states characterize the ends of each segment and are considered to be insulated from rest of the structure. The calculation of the states in the identification methodology proceeds from the root of the blade to the tip. Within

each analysis step from the station $n+1$ to station n , there are three intermediate steps.

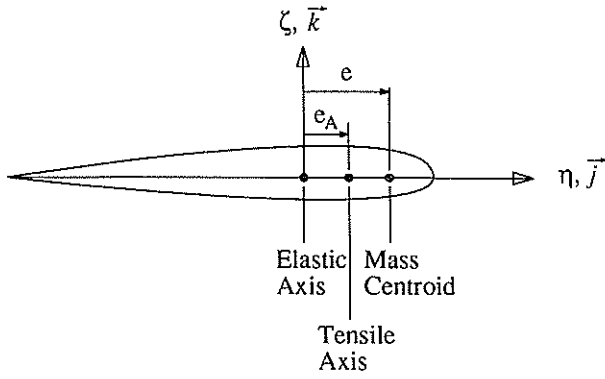


Fig. 4. Blade Structural Parameter Offsets

The first involves a rotation discontinuity $\Delta(\theta+\phi)_n$ between station $n+1$ and station n . This change in angle along the blade about the elastic axis accounts for the pre-twist built into the blade and the elastic deformation experienced by the blade. The blade pitch angle is

$$\theta_n = \theta_0 + \theta_{1c}\cos\psi + \theta_{1s}\sin\psi + \theta_{tw,n} \quad (1)$$

The second intermediate step, advancing from the left side of the segment to the right, involves movement across the massless elastic n th segment of length ℓ_n and the third involves movement across the n th lumped mass of the n th station. The second and third intermediate steps serve to establish the relationships of the forces and moments which act on the segment. Figure 5. shows the relative association of the discrete mass, elastic field and rotation for each segment.

Based on the process described above, the equations of motion in lumped parameter form, can be developed. To do so, the forces and moments that act on the n th blade segment are determined and the equilibrium of the segment in terms of a set of relations is obtained. These forces and moments are due to aerodynamic, inertia, centrifugal and Coriolis type loadings and couple with the deflection and slope relations through the elastic properties of the segment. Movement across the massless segment entails a coupling of the forces and moments on the segment through the elastic properties of the segment.

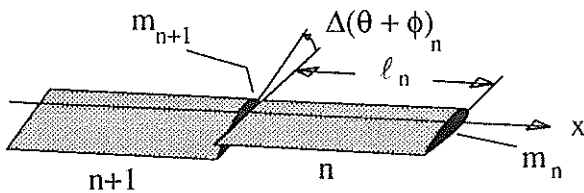


Fig. 5. Adjacent Blade Segments

Movement across the lumped mass involves only changes in the shear forces, bending moments and torque since there are no discontinuities in slopes or displacements. The equilibrium of the forces and moments, which include the external forces, and the elastic displacements and rotations at the n th blade

segment leads to the Eq. (2 to 11). These relations are structured in a loads identification manner and combine the last two steps in the analytical process of movement across the stiffness field and mass station. The equations of motion Eq. (2 to 11), in dimensional form, are as follows where, the script shear and moment parameters, S, \mathcal{M} signify terms due to inertia, centrifugal and Coriolis forces acting on the mass.

$$\bar{S}_{\zeta,n} = S_{\zeta,n} + \mathcal{S}_{\zeta,n} + F_{\zeta,n} \quad (2)$$

$$\begin{aligned} \bar{M}_{\eta,n} &= M_{\eta,n} + \bar{S}_{\zeta,n}\ell_n \\ &+ T_{n+1}(\bar{w}_n - w_n) + \mathcal{M}_{\eta,n} + \hat{M}_{\eta,n} \end{aligned} \quad (3)$$

$$\begin{aligned} \bar{w}'_n &= w'_n \left(1 + T_{n+1} \frac{\ell_n^2}{2EI_{\eta,n}} \right) - \bar{S}_{\zeta,n} \frac{\ell_n^2}{2EI_{\eta,n}} \\ &- \tilde{M}_{\eta,n} \frac{\ell_n}{EI_{\eta,n}} \end{aligned} \quad (4)$$

$$\begin{aligned} \bar{w}_n &= w_n - \bar{w}'_n \ell_n + T_{n+1} w'_n \frac{\ell_n^3}{3EI_{\eta,n}} \\ &- \bar{S}_{\zeta,n} \frac{\ell_n^3}{3EI_{\eta,n}} - \tilde{M}_{\eta,n} \frac{\ell_n^2}{2EI_{\eta,n}} \end{aligned} \quad (5)$$

$$\bar{S}_{\eta,n} = S_{\eta,n} + \mathcal{S}_{\eta,n} + F_{\eta,n} \quad (6)$$

$$\begin{aligned} \bar{M}_{\zeta,n} &= M_{\zeta,n} + \bar{S}_{\eta,n}\ell_n + T_{n+1}(\bar{v}_n - v_n) \\ &+ \mathcal{M}_{\zeta,n} + \hat{M}_{\zeta,n} - T_{n+1}e_{A,n} \end{aligned} \quad (7)$$

$$\begin{aligned} \bar{v}'_n &= v'_n \left(1 + T_{n+1} \frac{\ell_n^2}{2EI_{\zeta,n}} \right) - \bar{S}_{\eta,n} \frac{\ell_n^2}{2EI_{\zeta,n}} \\ &- \tilde{M}_{\zeta,n} \frac{\ell_n}{EI_{\zeta,n}} \end{aligned} \quad (8)$$

$$\begin{aligned} \bar{v}_n &= v_n - \bar{v}'_n \ell_n + T_{n+1} v'_n \frac{\ell_n^3}{3EI_{\zeta,n}} \\ &- \bar{S}_{\eta,n} \frac{\ell_n^3}{3EI_{\zeta,n}} - \tilde{M}_{\zeta,n} \frac{\ell_n^2}{2EI_{\zeta,n}} \end{aligned} \quad (9)$$

$$\bar{M}_{x,n} = M_{x,n} + \mathcal{M}_{x,n} + \hat{M}_{x,n} + M_{a,n} \quad (10)$$

$$\bar{\phi}_n = \phi_n - \frac{(\bar{M}_{x,n}\ell_n + T_{n+1}k_A^2\theta'_n\ell_n)}{(GJ_n + T_{n+1}k_A^2)} \quad (11)$$

where the centrifugal force is

$$T_{n+1} = T_n + m_n \Omega^2 r_n \quad (12)$$

The boundary conditions should be consistent with the identification analysis such that the bending and torsion moments are prescribed and the slopes may be prescribed depending on the hub configuration.

Parameters at the right edge of segment n+1 are advanced along the blade to the left edge of segment n using geometric transformations, provided in Eq. (13 to 22). Through these geometric transformation terms, nonlinearities exist due to the bending-torsion coupling.

$$\begin{aligned} \bar{S}_{\zeta,n} \cos(\Delta\theta_n + \Delta\phi_n) - \bar{S}_{\eta,n} \sin(\Delta\theta_n + \Delta\phi_n) \\ = S_{\zeta,n+1} \end{aligned} \quad (13)$$

$$\begin{aligned} \bar{M}_{\eta,n} \cos(\Delta\theta_n + \Delta\phi_n) - \bar{M}_{\zeta,n} \sin(\Delta\theta_n + \Delta\phi_n) \\ = M_{\eta,n+1} \end{aligned} \quad (14)$$

$$\begin{aligned} \bar{w}'_n \cos(\Delta\theta_n + \Delta\phi_n) - \bar{v}'_n \sin(\Delta\theta_n + \Delta\phi_n) \\ = w'_{n+1} \end{aligned} \quad (15)$$

$$\begin{aligned} \bar{w}_n \cos(\Delta\theta_n + \Delta\phi_n) - \bar{v}_n \sin(\Delta\theta_n + \Delta\phi_n) \\ = w_{n+1} \end{aligned} \quad (16)$$

$$\begin{aligned} \bar{S}_{\eta,n} \cos(\Delta\theta_n + \Delta\phi_n) + \bar{S}_{\zeta,n} \sin(\Delta\theta_n + \Delta\phi_n) \\ = S_{\eta,n+1} \end{aligned} \quad (17)$$

$$\begin{aligned} \bar{M}_{\zeta,n} \cos(\Delta\theta_n + \Delta\phi_n) + \bar{M}_{\eta,n} \sin(\Delta\theta_n + \Delta\phi_n) \\ = M_{\zeta,n+1} \end{aligned} \quad (18)$$

$$\begin{aligned} \bar{v}'_n \cos(\Delta\theta_n + \Delta\phi_n) + \bar{w}'_n \sin(\Delta\theta_n + \Delta\phi_n) \\ = v'_{n+1} \end{aligned} \quad (19)$$

$$\begin{aligned} \bar{v}_n \cos(\Delta\theta_n + \Delta\phi_n) + \bar{w}_n \sin(\Delta\theta_n + \Delta\phi_n) \\ = v_{n+1} \end{aligned} \quad (20)$$

$$\bar{M}_{x,n} = M_{x,n+1} \quad (21)$$

$$\bar{\phi}_n = \phi_{n+1} \quad (22)$$

Relations which couple the moment, deflection and slope terms, presented as Eq. (2 to 5) and Eq. (6 to 9) along with the moment transformation Eq. (14 and 18), can be reformulated to develop an 8x8 transfer matrix. From this process, it can be seen that the unknown shears, which are transferred along the blade, can be determined at segment n as a function of blade displacements, deflections and moments. This approach is an inverse of the response approach in which the shears are determined from the "known" airloads. Through the identification process, the torsional

moments along the blade are considered known and as such the torsional displacements can be determined along the blade in a manner independent of the coupled flap and lag relations using Eq. (28). It is noted in this analysis, the structural coupling terms identified by Mil' *et al.* [7], which couple the bending with the torsion through the product of the curvatures are not included. These nonlinear terms should be incorporated for the hingeless rotor configuration and for the case where bending stiffnesses are not "closely matched".

$$\begin{aligned} \bar{M}_{\eta,n} - \bar{S}_{\zeta,n} \ell_n + T_{n+1} w_n - \Omega^2 I_{\eta,n} (w'_n + v_n \theta'_n) \\ + I_{\eta,n} (\dot{w}'_n + \dot{v}_n \theta'_n) = M_{\eta,n} + T_{n+1} \bar{w}_n \end{aligned} \quad (23)$$

$$\begin{aligned} + 2\Omega I_{\eta,n} ((\dot{\phi}_n + \dot{\theta}_n) \cos\theta_n - \dot{\theta}_n \phi_n \sin\theta_n) \\ + (\bar{U}_{\eta,n-1} \cos\Delta\theta_{n-1} - \bar{U}_{\zeta,n-1} \sin\Delta\theta_{n-1}) (\phi_n - \phi_{n-1}) \end{aligned}$$

$$\begin{aligned} \bar{M}_{\zeta,n} - \bar{S}_{\eta,n} \ell_n + T_{n+1} v_n - \Omega^2 I_{\zeta,n} (v'_n - w_n \theta'_n) \\ + I_{\zeta,n} (\dot{v}'_n - \dot{w}_n \theta'_n) \\ + 2m_n \Omega e_n (-\dot{w}_n \sin\theta_n + \dot{v}_n \cos\theta_n) \\ - 2m_n \Omega e_n \dot{\theta}_n (w_n \cos\theta_n + v_n \sin\theta_n) = \end{aligned} \quad (24)$$

$$\begin{aligned} M_{\zeta,n} + T_{n+1} \bar{v}_n - m_n \Omega^2 r_n e_n \\ + 2\Omega I_{\zeta,n} ((\dot{\phi}_n + \dot{\theta}_n) \sin\theta_n + \dot{\theta}_n \phi_n \cos\theta_n) \\ + (\bar{U}_{\zeta,n-1} \cos\Delta\theta_{n-1} + \bar{U}_{\eta,n-1} \sin\Delta\theta_{n-1}) (\phi_n - \phi_{n-1}) \\ - T_{n+1} e_{A,n} \end{aligned}$$

$$\begin{aligned} v'_n \left(1 + T_{n+1} \frac{\ell_n^2}{2EI_{\zeta,n}} \right) - \bar{S}_{\eta,n} \frac{\ell_n^2}{2EI_{\zeta,n}} \\ - \left(\Omega^2 I_{\zeta,n} (v'_n - w_n \theta'_n) - I_{\zeta,n} (\dot{v}'_n - \dot{w}_n \theta'_n) \right. \\ - 2m_n \Omega e_n (-\dot{w}_n \sin\theta_n + \dot{v}_n \cos\theta_n) \\ \left. - \dot{\theta}_n (w_n \cos\theta_n + v_n \sin\theta_n) \right) \frac{\ell_n}{EI_{\zeta,n}} = \bar{v}'_n \end{aligned} \quad (25)$$

$$\begin{aligned} + \left(M_{\zeta,n} - m_n \Omega^2 r_n e_n + 2\Omega I_{\zeta,n} ((\dot{\phi}_n + \dot{\theta}_n) \sin\theta_n \right. \\ + \dot{\theta}_n \phi_n \cos\theta_n) + (\bar{U}_{\zeta,n-1} \cos\Delta\theta_{n-1} \\ \left. + \bar{U}_{\eta,n-1} \sin\Delta\theta_{n-1}) (\phi_n - \phi_{n-1}) - T_{n+1} e_{A,n} \right) \frac{\ell_n}{EI_{\zeta,n}} \end{aligned}$$

$$\begin{aligned}
& w_n + T_{n+1}w'_n \frac{\ell_n^3}{3EI_{\eta,n}} - \bar{S}_{\zeta,n} \frac{\ell_n^3}{3EI_{\eta,n}} \\
& - \left(\Omega^2 I_{\eta,n} (w'_n + v_n \theta'_n) - I_{\eta,n} (\dot{w}_n \right. \\
& \left. + v_n \dot{\theta}_n) \right) \frac{\ell_n^2}{2EI_{\eta,n}} = \bar{w}_n + \bar{w}'_n \ell_n + (M_{\eta,n} \\
& + 2\Omega I_{y,n} ((\dot{\phi}_n + \dot{\theta}_n) \cos \theta_n - \dot{\theta}_n \phi_n \sin \theta_n) \\
& + (\bar{U}_{\eta,n-1} \cos \Delta \theta_{n-1} - \bar{U}_{\zeta,n-1} \sin \Delta \theta_{n-1}) \\
& (\phi_n - \phi_{n-1}) \frac{\ell_n^2}{2EI_{\eta,n}}
\end{aligned} \tag{26}$$

$$\begin{aligned}
& v_n + T_{n+1}v'_n \frac{\ell_n^3}{3EI_{\zeta,n}} - \bar{S}_{\eta,n} \frac{\ell_n^3}{3EI_{\zeta,n}} \\
& - \left(\Omega^2 I_{\zeta,n} (v'_n - w_n \theta'_n) - I_{\zeta,n} (\dot{v}_n - \dot{w}_n \theta'_n) \right. \\
& \left. - 2m_n \Omega e_n ((-\dot{w}_n \sin \theta_n + \dot{v}_n \cos \theta_n) - \dot{\theta}_n (w_n \cos \theta_n) \right. \\
& \left. + v_n \sin \theta_n) \right) \frac{\ell_n^2}{2EI_{\zeta,n}} = \bar{v}_n + \bar{v}'_n \ell_n \\
& + (M_{\zeta,n} - m_n \Omega^2 r e_n + 2\Omega I_{\zeta,n} ((\dot{\phi}_n + \dot{\theta}_n) \sin \theta_n \\
& + \dot{\theta}_n \phi_n \cos \theta_n) \\
& + (\bar{U}_{\zeta,n-1} \cos \Delta \theta_{n-1} + \bar{U}_{\eta,n-1} \sin \Delta \theta_{n-1}) \\
& (\phi_n - \phi_{n-1}) - T_{n+1} e_{A,n} \frac{\ell_n^2}{2EI_{\zeta,n}}
\end{aligned} \tag{27}$$

$$\phi_n = \phi_{n+1} + \frac{(M_{x,n+1} \ell_n + T_{n+1} k_A^2 \theta'_n \ell_n)}{(GJ_n + T_{n+1} k_A^2)} \tag{28}$$

Along with the torsional response ϕ_n , the flatwise w_n , and edgewise v_n , responses of the blade can be identified for each blade segment. The steady and unsteady airloads depend on the blade response and will be used in the identification of the inflow and components of the drag.

With the shears having been determined for an n th blade segment, the external loads in the principal axes system, $F_{\zeta,n}$, $F_{\eta,n}$ and $M_{a,n}$ can be identified. These relationships, derived from Eq. (2, 6 and 10), are provided in Eq. (29 to 31). In this analysis only the steady state solutions are sought. It is therefore assumed that the steady state response of a rotor blade is periodic so a harmonic solution is applied to the equations of motion. These harmonics are of the form $a_{\kappa c} \cos(\kappa \Omega t) + a_{\kappa s} \sin(\kappa \Omega t)$ and result in a separate set of complex identified parameters for each κ harmonic.

$$\begin{aligned}
F_{\zeta,n} &= \bar{S}_{\zeta,n} - S_{\zeta,n} + m_n \dot{w}_n \\
&+ m_n \Omega^2 \sin \theta_n (-w_n \sin \theta_n + v_n \cos \theta_n + e_n \cos \theta_n \\
&+ e_o) - m_n \Omega^2 e_n \phi_n (\sin^2 \theta_n \\
&- \cos^2 \theta_n) + m_n \Omega^2 e_o \phi_n \cos \theta_n + m_n e_n (\ddot{\phi}_n + \ddot{\theta}_n) \\
&+ 2m_n \Omega \sin \theta_n \left[e_n (\dot{v}_n - \dot{w}_n \theta'_n) \right. \\
&\left. + \int_0^{\ell_n} (w'_n \dot{w}'_n + v'_n \dot{v}'_n) dr \right]
\end{aligned} \tag{29}$$

$$\begin{aligned}
F_{\eta,n} &= -\bar{S}_{\eta,n} + S_{\eta,n} - m_n \dot{v}_n \\
&+ m_n \Omega^2 \cos \theta_n (-w_n \sin \theta_n + v_n \cos \theta_n \\
&+ e_n \cos \theta_n + e_o) - 2m_n \Omega^2 e_n \phi_n \sin \theta_n \cos \theta_n \\
&- m_n \Omega^2 e_o \phi_n \sin \theta_n \\
&+ 2m_n \Omega \cos \theta_n \left[e_n (\dot{v}_n - \dot{w}_n \theta'_n) \right. \\
&\left. + \int_0^{\ell_n} (w'_n \dot{w}'_n + v'_n \dot{v}'_n) dr \right]
\end{aligned} \tag{30}$$

$$\begin{aligned}
M_{a,n} &= M_{x,n+1} - M_{x,n} + m_n \Omega^2 e_n r_n w'_n \\
&- (\bar{U}_{\zeta,n-1} \cos \Delta \theta_{n-1} + \bar{U}_{\eta,n-1} \sin \Delta \theta_{n-1}) w'_n \\
&- \bar{U}_{\eta,n-1} w'_{n-1} + m_n \Omega^2 e_n ((-w_n \sin \theta_n \\
&+ v_n \cos \theta_n + e_o) \sin \theta_n + e_o \phi_n \cos \theta_n) \\
&+ m_n e_n \dot{w}_n + \Omega^2 (I_{\zeta,n} - I_{\eta,n}) \phi_n \cos 2\theta_n \\
&+ (I_{\zeta,n} - I_{\eta,n}) \sin \theta_n \cos \theta_n + I_{\theta,n} (\ddot{\phi}_n + \ddot{\theta}_n) \\
&+ 2\Omega I_{\eta,n} (\dot{w}_n + v_n \theta'_n) \cos \theta_n \\
&+ 2\Omega I_{\zeta,n} (\dot{v}_n - \dot{w}_n \theta'_n) \sin \theta_n \\
&+ 2m_n \Omega e_n \sin \theta_n \int_0^{\ell_n} (w'_n \dot{w}'_n + v'_n \dot{v}'_n) dr
\end{aligned} \tag{31}$$

Aerodynamic Force and Inflow Identification Model

The identified external loadings, $F_{\zeta,n}$, $F_{\eta,n}$ and $M_{a,n}$, in the principal axes system, can now be used in the identification of the airloads and the corresponding inflow. The airloads must be represented in the wind axes system to correctly identify the lift, drag, aerodynamic pitching moment and inflow at a given blade segment. To accomplish this, an iteration scheme is devised to transform the loads into the wind axes using the identified loads in conjunction with two-dimensional wind tunnel data and the identified blade response data. The orientation of the wind relative to the blade section,

as influenced by flight condition, is important so yawed flow effects are considered.

The aerodynamic environment encompassing the rotor blade can be divided into two problems noted as the "inner" and "outer" problems. The inner problem addresses the force theories at the airfoil and the outer problem addresses the rotor wake. In the traditional airload prediction sense, rotor blade airloads are implicitly determined as a consequence and condition for rotor trim. This is necessary since the rotor inflow and associated geometry are unknown and as a result, the aerodynamic environment at the blade segment, or inner problem, cannot be explicitly determined. At this point in airloads prediction methodology, a wake model with an assumed or determined geometry would be coupled with the airloads model to provide a closed form set of equations. However, with identification methodology, the airloads in the cross-sectional axes of the blade are determined independent of the wake. In fact, knowing the airloads implies that the inflow due to the shed and trailed wake are known; and, consequently, the nonuniform steady and unsteady inflow can be identified at the blade segment through the transformation of these loads into the wind axes. In the identification methodology, no assumptions need be made regarding the wake or its geometry since the known airloads explicitly contain this information. To obtain the airloads and inflow at a blade segment, two first-order airload theories, steady lifting-line theory and unsteady thin airfoil theory, are used in this analysis. These theories, as used, make no assumptions regarding the wake and allow for the wake and airloads to be treated separately. Lifting-line theory (i.e. strip theory or blade element theory) was chosen in lieu of lifting-surface theory for the steady loads because of its simplicity,

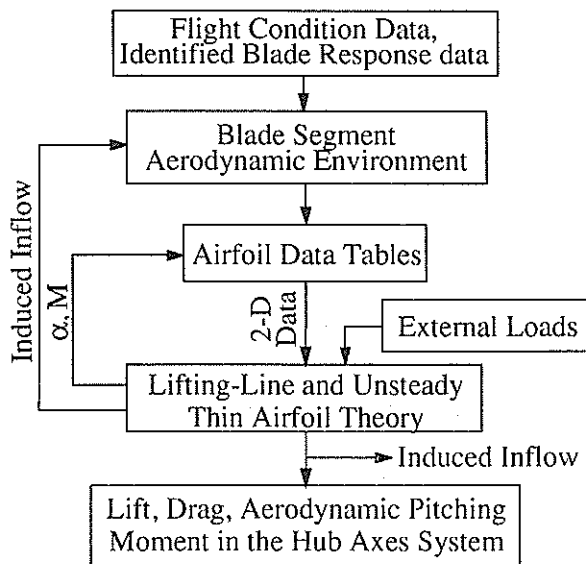


Fig. 6. Rotor Blade Airload and Inflow Identification Process at nth Blade Station

computational efficiency and adaptability to the identification process. This theory is linear and, under certain conditions, applicable to two-dimensional incompressible flows. Lifting-line theory is well suited for the identification process in that the external normal load is known. Thus, the circulation on the blade, due to the trailing vortex system, can be identified by correctly

describing the aerodynamic environment at that blade section. Lifting-line theory, which is a finite wing theory, uses a single bound vortex, placed at the aerodynamic center, running the span of the blade and assumes that the aerodynamic environment varies slowly along the blade. This assumption is usually well satisfied for the rotor blade, given the fact that it is long and slender. The assumption, however, is not satisfied near the blade tip and along the section of the blade where a close vortex interaction occurs. In these situations, three-dimensional flow and large changes in the aerodynamic environment exist. The lift near the tip is usually corrected using some type of tip loss factor. However, because the lift has been identified a priori, using this correction is not applicable. Still, three-dimensional flow is present and thus the determination of angle of attack, inflow, etc. will incur some loss in accuracy. The loads on the blade associated with a blade vortex interaction are not included in the model.

The aerodynamic model is applicable for a range of flight conditions including hover and forward flight, and low and high inflow conditions. Compressible flow and yawed flow corrections are incorporated and reverse flow is included. From this theory, the aerodynamic loads per unit length in the wind axes system can be expressed as

$$\begin{aligned} L_n &= 1/2\rho u_n^2 c_n C_l(\alpha_e, M_e) \\ D_n &= 1/2\rho u_n^2 c_n C_d(\alpha_e, M_e) \\ M_{apm,n} &= -x_{ac,n} L_n + M_{ac,n} = \\ &= 1/2\rho u_n^2 c_n (-x_{ac,n} C_l(\alpha_e, M_e) + c_n C_m(\alpha_e, M_e)) \end{aligned} \quad (32)$$

where

$$\begin{pmatrix} u_R \\ u_T \\ u_P \end{pmatrix} = \Omega \begin{pmatrix} \mu R \cos \psi \\ r + \mu R \sin \psi \\ R(\lambda_m + \mu \tan \alpha_{HP}) \end{pmatrix} \quad (33)$$

and the effective angle of attack is

$$\alpha_e = \theta_T - \frac{\lambda R}{r} - \frac{v}{r} w' + v' w' - \int_0^r v'' w' dr \quad (34)$$

The steady lift in the wind axes system is identified by employing the previously determined external loads, F_{η} , F_{ζ} , in addition to two-dimensional lift coefficient data. The resultant relative velocity, u , is rotated relative to the blade segment to satisfy the solutions for the effective angle of attack and the inflow angle, ϕ relationship. In this rotation, the lift vector remains perpendicular to u . A physical constraint is placed on the process through the use of C_l which depends on a combination of the angle of attack, Mach number and yawed/swept flow. The process to identify the inflow is implicit and a binary-search iteration scheme is used to obtain all of the parameters related to the aerodynamic environment. The process is started with an initial value specified for the inflow where the inflow is iterated until the error, ϵ , in the solution, Eq. (35) is forced to zero.

$$\varepsilon = 1/2\rho u_{\infty}^2 c_n C_{\ell} - F_{\zeta,n} \cos \alpha_{e,n} - F_{\eta,n} \sin \alpha_{e,n} \quad (35)$$

A rotor blade, subjected to a time varying free stream and/or unsteady motion, requires an analysis employing unsteady aerodynamics. These unsteady airloads, which are characterized by heave and pitch motion of the blade and a time varying free stream, are obtained using thin airfoil theory which is extended for rotary wing application [8]. This theory is linear and is applicable to two-dimensional incompressible potential flows.

The airfoil is assumed to be a flat plate with zero thickness and having a chord length $2b$. The airfoil experiences arbitrary heave motion, w in the z direction and pitch motion θ about the elastic axis. The relative air velocity in the y direction is denoted as U_T . A relative air velocity component, normal to the airfoil, is created and defined as $w_b + v_w$, which is the total downwash due to a vorticity distribution along the airfoil. The velocity due to blade motion w_b , is defined as positive up and the wake induced inflow v_w is defined as positive down. The blade velocity is written as a mean value plus a term linear in y , $w_b = -(A + By)$ and the induced velocity is expanded in a Glauert series over the blade chord, where $A = -\dot{w} + U_T \dot{\theta}$ and the rate

of blade pitch and torsional deformation, $B = \dot{\theta}$. To obtain the lift and pitching moment on the airfoil, the pressure differential across the airfoil may be determined with the use of the linearized form of Kelvin's equation. The pressure differential can then be integrated across the chord to obtain the unsteady lift and moment. The lift and moment equations can be expressed in terms of blade motion and inflow coefficients to provide the unsteady loads for the rotary wing case. These load relationships are presented in a form where the circulatory and noncirculatory terms are separated as necessary for the identification methodology. These equations consist of higher order and time dependent inflow terms. Because the inflow is calculated at one point on the blade, it is desirable to assume and employ a flat wake approximation [8] to obtain the inflow in terms of only v_0 .

$$L_{zc} = a |U_T| \frac{c}{2} \rho \left[A - v \pm \frac{c}{2} B \left(1 \pm \frac{2x_{ac}}{c} \right) \right] \quad (40)$$

$$L_{znc} = a \frac{c^2}{8} \rho \left[\dot{A} + \dot{B} \left(\pm \frac{c}{4} + x_{ac} \right) \right] \quad (41)$$

$$L_{yc} = -a \frac{c}{2} \rho \left[A - v \pm \frac{c}{2} B \left(1 \pm \frac{2x_{ac}}{c} \right) \right]^2 \quad (42)$$

$$M_{ac} = -a |U_T| \frac{c^2}{4} \rho \left[\pm \frac{2x_{ac}}{c} (A - v) \pm \frac{c}{8} B \left(1 \pm \frac{4x_{ac}}{c} \right)^2 \right] \quad (43)$$

$$M_{anc} = \mp a \frac{c^3}{32} \rho \left[\left(1 \pm \frac{4x_{ac}}{c} \right) \dot{A} \pm \frac{c}{16} \dot{B} \left(1 + 2 \left(1 \pm \frac{4x_{ac}}{c} \right)^2 \right) \right] \quad (44)$$

The lift curve slope and the location of aerodynamic center were corrected using two-dimensional experimental data, where the flow is compressible. The induced velocity is identified at a blade segment as a function of the identified unsteady lift load, the corresponding blade motion and the relative air velocity at the blade section. The total identified unsteady lift is comprised of both circulatory and noncirculatory terms. The noncirculatory terms, which are due to blade motion, are separated from the identified unsteady lift yielding only the circulation due to blade motion and shed-wake induced velocity.

$$L_{zc} = L_z - L_{znc} \quad (45)$$

The identified and noncirculatory lift terms are determined in the principal axes system yielding the net circulatory lift in the same reference frame. While the boundary condition is satisfied through the noncirculatory vorticity, an error exists however, Eq. (42), in the required unsteady circulatory vorticity due to the motion of the blade and shed wake. In a manner analogous to the steady lift, the unsteady circulatory lift term needs to be iterated on the unsteady shed-wake induced velocity in order to satisfy the total bound vorticity requirement. A binary-search iteration scheme is again employed for this process. To satisfy the total bound circulation requirement, the resultant velocity vector at the three quarter chord point is rotated through the angle of attack, α , using the blade motion and iterated inflow values. During the rotation, the circulatory lift remains perpendicular to the resultant velocity.

$$\varepsilon = a |U_T| \frac{c}{2} \rho \left[(A - v) \pm \frac{c}{2} \left(1 \pm \frac{2x_{ac}}{c} \right) B \right] - (F_{\zeta} - L_{znc}) \cos \alpha - F_{\eta} \sin \alpha \quad (46)$$

As with the results from the blade load identification, the results from the aerodynamic forces and inflow are presented in harmonic form. Figure 6. provides an overview of the airloads in the wind axes and inflow identification process.

Results and Discussion

The UH-60A main rotor was used as the model in the verification of the method and the identification analysis. Airloads data from the NASA/Army UH-60A Black Hawk Airloads Program (BHAP) were used in the analysis and two flight speeds were considered, $\mu=0$. and $\mu=.193$ along with corresponding air density and rotor speed data. References [9 and 10] provide highlights of the test program.

The flap and lag elastomeric bearing and torsion bearing was assumed to be co-located and the main rotor blade was discretized into 48 spanwise elements for a total of 49 radial stations. The outer 48 radial stations along the blade, $r=.06R$ to $1.0R$, were equally spaced

while the 49th station was placed at .0466R to coincide with the focal point of the elastomeric bearing. The lengths of the outer 47 elements is $l = .02R$ and the inner most element between station 48 and 49 has a length of $l = .0134R$. The built-in blade twist, which washes out in a linear manner for most of the blade, has a positive slope beyond .94R. The control system stiffness, k_{ϕ} , was assumed to be linear. The UH-60A main rotor blade has an aft swept tip which was ignored in the analysis.

In the analysis, it is desirable to use bending-torsional moments obtained from experimental strain measures to determine the spanwise external moments. However, due to various limitations in the BHAP strain measure data, these data were not utilized. Consequently, to obtain the distributed bending and torsional moments and blade root angles, simulation was used and to generate these data sets, a prediction methodology was employed. The simulated distributed bending-torsional

Table 1. Comparison of Eigenvalues: Transfer Matrix Method (TMM) vs. CAMRAD/JA, Coupled Bending Modes (Per Rev), $\theta_{.75R} = 16$. deg.

	TMM	CAMRAD/JA
Mode	Bending	Bending
1	0.268	0.269
2	1.035	1.036
3	2.807	2.808
4	4.696	4.691
5	5.170	5.174
6	7.831	7.863
7	11.442	11.526
8	12.660	12.605
9	15.830	15.950
10	21.218	21.391

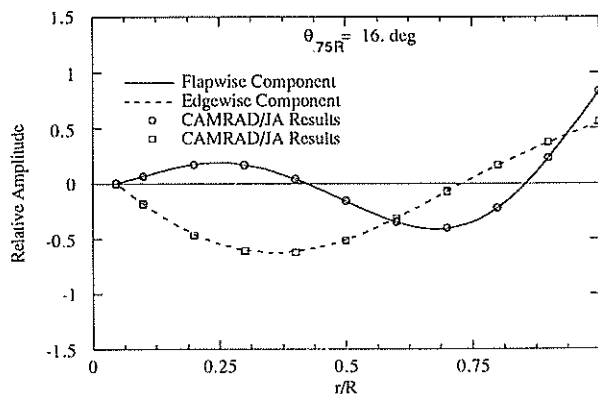


Fig. 7. Modal Analysis: Transfer Matrix Method vs. CAMRAD/JA, 4th Coupled Bending Mode

moments and blade root angles were generated using the bending-torsion equations from Ref. [3] in the form of the Transfer Matrix Method (TMM) where the BHAP airloads data were used as the forcing function. To validate this structural dynamics model, the modes and frequencies from the prediction analysis were checked for agreement with the results from CAMRAD/JA, Ref. [11]. Table 1. provides the Eigenvalues and Fig. 7., the

Eigenvectors for the bending case, respectively. Table 2. and Fig. 8. provide the Eigenvalues and Eigenvectors, respectively, for the torsion case. The identification analysis only considered the first 10 harmonics (including the steady term) and the TMM correlates very well for this frequency range.

Table 2. Comparison of Eigenvalues: Transfer Matrix Method (TMM) vs. CAMRAD/JA, Torsion Modes (Per Rev), Rigid Root

	TMM	CAMRAD/JA
Mode	Torsion	Torsion
1	5.333	5.357
2	4.895	4.905
3	15.657	15.109
4	25.992	25.098
5	36.444	36.765
6	47.755	50.813
7	67.681	69.645
8	##	##
9	##	##
10	##	##

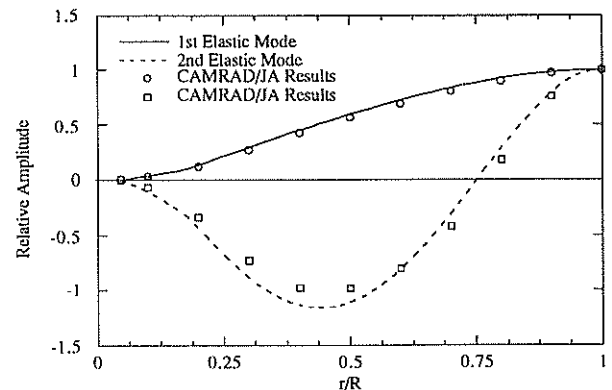


Fig. 8. Modal Analysis: Transfer Matrix Method vs. CAMRAD/JA, 1st and 2nd Elastic Torsion Modes, Rigid Root

The identification process of the rotor blade's external moments depends on, among other things, the accurate identification of the blade's displacements. To obtain confidence in the identified moments and the methodology itself, a second validation exercise was conducted at a midpoint in the solution process. As such, the identified blade displacements were correlated with the simulated data from the response methodology. The identification methodology for the UH-60A employed the simulation data for the flight conditions, $\mu=0$. and $\mu=0.193$. For each respective flight condition, the identification analysis was performed at two rotor azimuthal positions, $\psi=0$. and $\psi=90$. deg. Figures 9. and 10. provide examples for the steady and first harmonic cosine displacement coefficients at $\mu=0$. One set of parameter curves, in each figure, are the simulated data and are considered to be an "exact" set of measurements which are labeled as "Data" and are referred to as "measured data". The other set of parameter curves are the data generated from the identification methodology

and are labeled as "Identification". Each curve is comprised of 49 radially distributed data points and the placement of the symbol markers is without significance. As can be seen, the correlation between the measured data and the identified results are excellent.

The results from the analysis of the distributed external forces and moments are next correlated with experimental flight test data from the UH-60A flight test program as

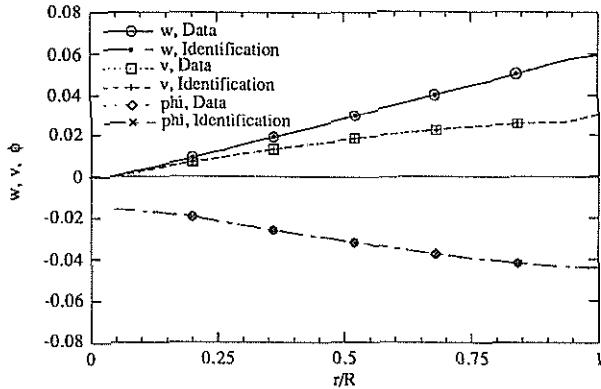


Fig. 9. Nondimensionalized Flatwise and Chordwise Displacements and Torsional Displacement, Zeroth Harmonic, $\mu=0$.

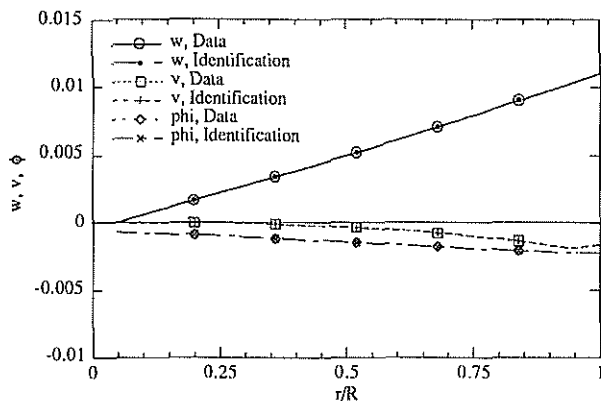


Fig. 10. Nondimensionalized Flatwise and Chordwise Displacements and Torsional Displacement, First Harmonic, $\mu=0$, $\psi=0$ deg.

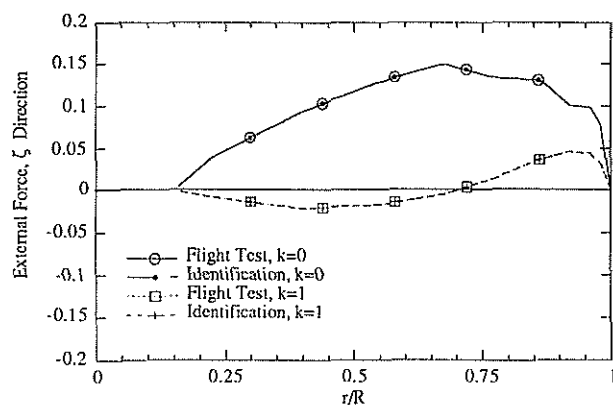


Fig. 11. Nondimensionalized Identified External Force, ζ Direction, Zeroth and First Harmonic, $\mu=.193$, $\psi=0$ deg.

shown in Fig. 11. through 16. A range of harmonics at $\mu=.193$ and $\psi=0$ deg. are shown. In each figure, one set of parameter curves are the UH-60A airloads flight test data which are an exact set of measurements and are labeled as "Flight Test". The other set of parameter curves are the corresponding external moments generated from the identification methodology and are labeled as "Identification". The external forces and moments, in per

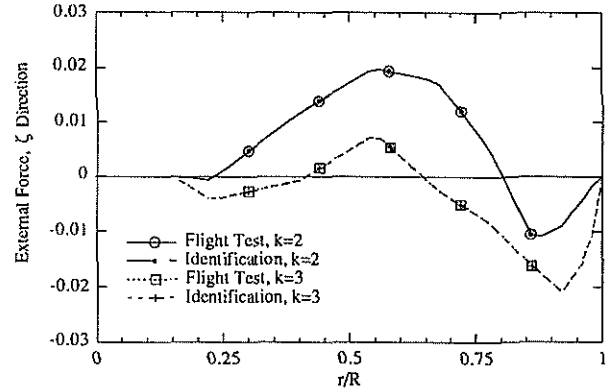


Fig. 12. Nondimensionalized Identified External Force, ζ Direction, Second and Third Harmonic, $\mu=.193$, $\psi=0$ deg.

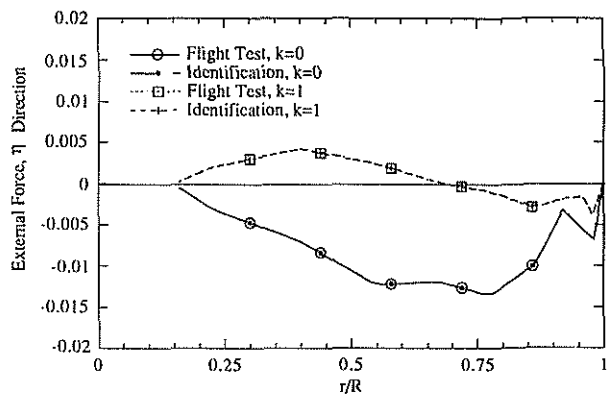


Fig. 13. Nondimensionalized Identified External Force, η Direction, Zeroth and First Harmonic, $\mu=.193$, $\psi=0$ deg.

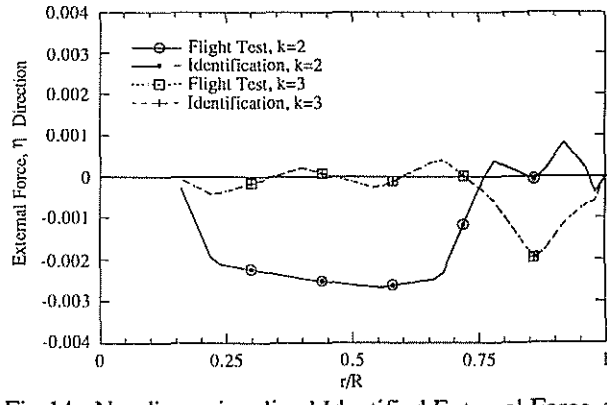


Fig. 14. Nondimensionalized Identified External Force, η Direction, Second and Third Harmonic, $\mu=.193$, $\psi=0$ deg.

unit length in the analysis, have been nondimensionalized for presentation by the factors $\rho(\Omega R)^2 \bar{c}$ and $\rho(\Omega R)^2 \bar{c}^2$, respectively. Again, it can be seen that the correlation between the flight test data and the identified results are excellent.

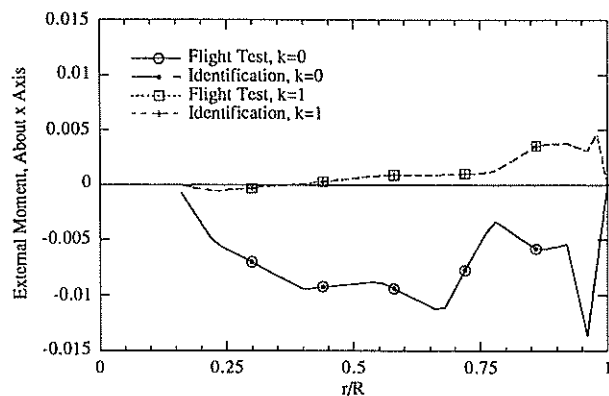


Fig. 15. Nondimensionalized Identified External Moment About x Axis, Zeroth and First Harmonic, $\mu=.193$, $\psi=0$. deg.

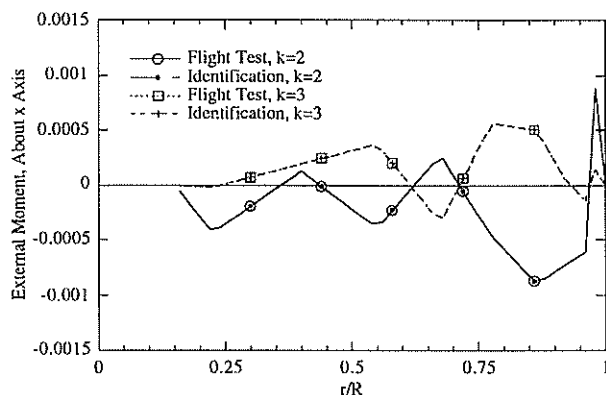


Fig. 16. Nondimensionalized Identified External Moment About x Axis, Second and Third Harmonic, $\mu=.193$, $\psi=0$. deg.

The results, as shown, indicate that the flatwise and chordwise shears are correctly identified in the analysis since the external forces are dependent upon the shears. Through the blade response and external load identification analysis it has been shown that the identification methodology is properly posed and that solution process is correct. It was shown that the correlation is excellent between the simulated and identified displacements. Finally, the correlation is excellent between the identified and experimental airloads and it is reasonable to conclude that the identification process for external loads and moments has been validated. It is also concluded that the identified external loads are suitable for use in the identification of the airloads in the wind axes, the corresponding induced inflow.

The identification of airloads and inflow identification methodology in the wind axes system is now considered. It is noted that experimental data are unavailable to directly compare with any of these

identified spanwise parameters, and as such, the figures are presented for examination of the methodology and process. The methodology employed the identified external loads data for the flight condition $\mu=0.193$ and $\psi=0$. deg. Also, only the first six harmonics (including the zeroth harmonic) have been analyzed. The first and higher harmonics of the sectional lift and aerodynamic pitching moment combined the circulatory terms and noncirculatory terms to give the total load for the particular harmonic.

The induced inflow is presented in nondimensional form as, $v/\Omega R$. The aerodynamic forces and pitching moment been nondimensionalized by the factors $\rho(\Omega R)^2 \bar{c}$ and $\rho(\Omega R)^2 \bar{c}^2$, respectively. The radial distribution is presented for each of the evaluated parameters and each curve is comprised of 49 radially distributed data points.

These inflow examples, Fig. 17. and 18., show the longitudinal inflow variation (aft portion) results for the forward flight case and present the harmonics of the radially distributed induced flow. The inflow results that are presented throughout the analysis are the total induced flow (momentum + forward flight component). The angle of attack of the hub plane was considered for the forward flight condition using the fuselage Euler angle from flight test and the rotor shaft geometric data. Because the induced flow plays an important role in the identification of the airloads on the blade, it was desired to present the summation of the first ten harmonics, including the steady coefficient. It is noted from these figures, the reduction in magnitude of the induced flow near $r=.95R$, particularly for the zeroth harmonic. This phenomenon is probably due to the trailed vortex at the blade tip. It is further noted that at the blade root and tip, in addition to the lift, drag and aerodynamic pitching moment being zero, the relative air flow is highly three-dimensional and as such the inflow values are not accurate at these and neighboring radial locations. The positive induced flow indicates the blade is flapping up which corroborates the flight test data, $\beta_{1c}=2.34$ and $\beta_{1s}=1.19$ deg. As can be seen from the forward flight case, the first and higher harmonics of the induced flow, are relatively large in magnitude. Especially the first harmonic which is of the same order of magnitude as the zeroth harmonic, a necessary result for the helicopter to maintain forward flight.

The aerodynamic loads in the wind axes are shown in Fig. 19. to 23. which provide the results for the case $\mu=.193$ at $\psi=0$. deg. The sectional lift were obtained by rotating the external pressure forces into the wind axes as previously discussed. The sectional lift in Fig. 19 and 20. are very similar in magnitude and shape to the Fig. 11. and 12. as expected. This is the case since the product $F_{\eta} \sin \alpha_e$, when not in the stall regime, is second order small and consequently has a small influence on the lift. It is important, however, to not discard the $F_{\eta} \sin \alpha_e$ term since in the steady stall condition, its role becomes increasingly important. This assumes that the airfoil tables utilized in the analysis are valid for high angles of attack. The steady sectional drag is shown in Fig. 21. where the sectional drag is defined as positive aft. Of the harmonics, only the steady sectional drag term is

presented since the magnitudes of the higher harmonics are exceedingly small for presentation. In Figures 21. and 22., the aerodynamic pitching moments are shown. This parameter was generated using the lift in the wind axes, the pitching moment at the aerodynamic center and aerodynamic center offset data. Because the available aerodynamic center offset data is constant with angle of attack, large discrepancies exist between the external pitching moment, M_a , in Fig. 15. and 16. and the corresponding cases of $M_{a_{pm}}$ for the radial region where the angle of attack on the blade is relatively large, namely

the inner half of the blade radius.

The identified results, in general, have an excellent correlation with the experimental data provided therein. However, since random errors, in the form of noise, in the simulated data does not exist, the results are not fortuitous and are an inevitable outcome. Since it is well known that the experimental measurements are an important basis for identification, an error analysis was performed to evaluate the robustness of the identification method. Two error analyses was performed. The first, in

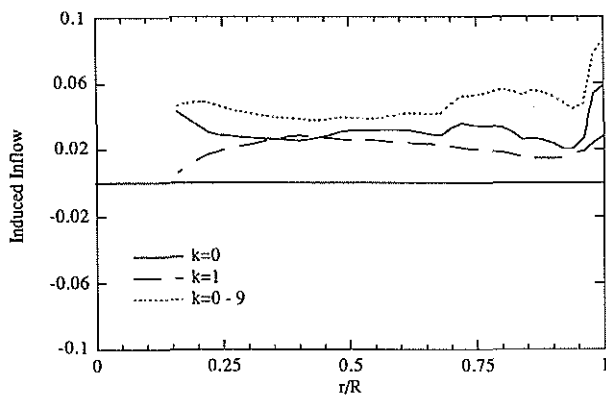


Fig. 17. Nondimensionalized Identified Induced Flow, Zero, First and Summed Zero Through Ninth Harmonics, $\mu=.193$, $\psi=0$. deg.

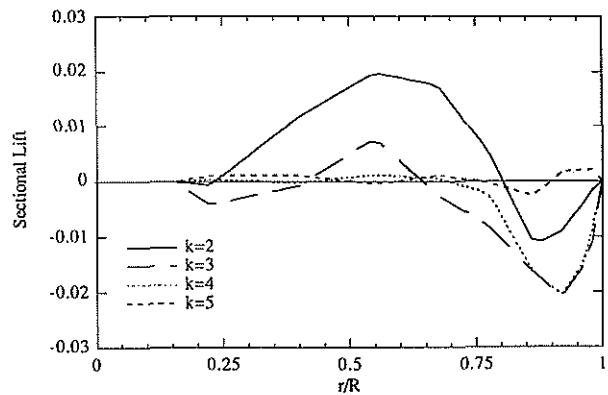


Fig. 20. Nondimensionalized Identified Lift, Second Through Fifth Harmonic, $\mu=.193$, $\psi=0$. deg.

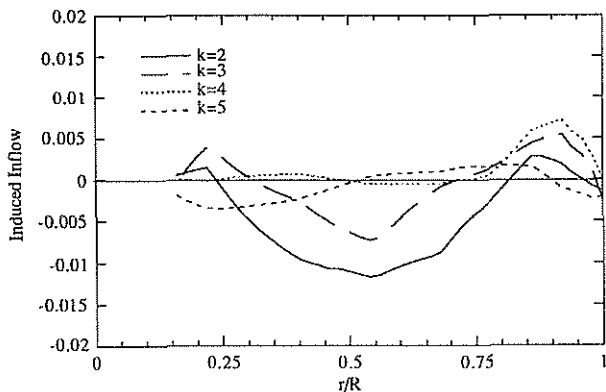


Fig. 18. Nondimensionalized Identified Induced Flow, Second Through Fifth Harmonic, $\mu=.193$, $\psi=0$. deg.

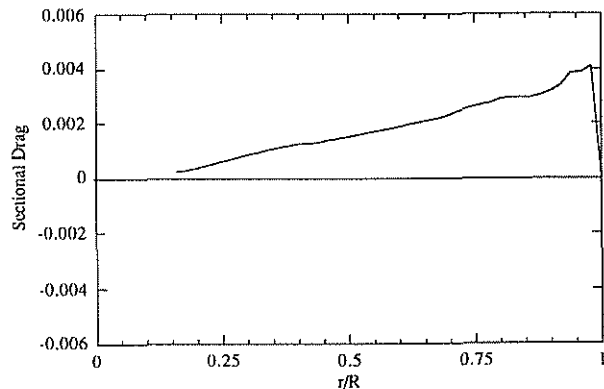


Fig. 21. Nondimensionalized Identified Drag, Zeroth Harmonic, $\mu=.193$

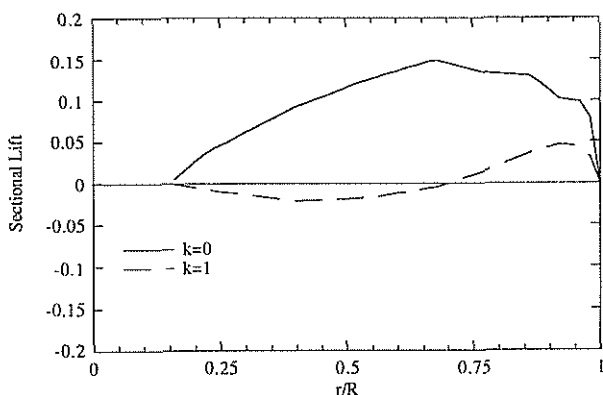


Fig. 19. Nondimensionalized Identified Lift, Zeroth and First Harmonic, $\mu=.193$, $\psi=0$. deg.

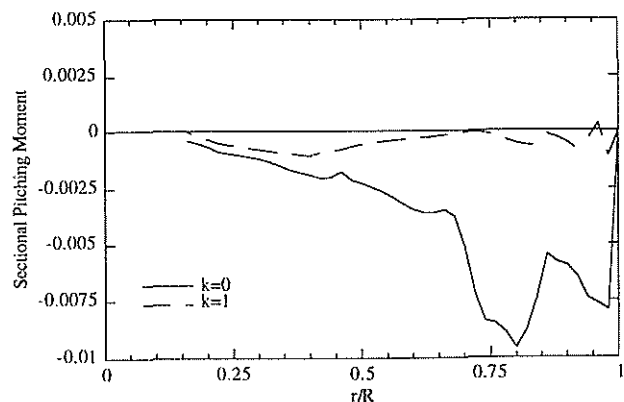


Fig. 22. Nondimensionalized Identified Aerodynamic Pitching Moment, Zeroth and First Harmonic, $\mu=.193$, $\psi=0$. deg.

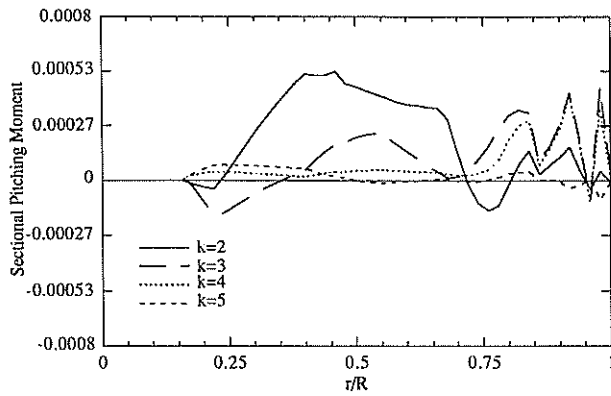


Figure 23. Nondimensionalized Identified Aerodynamic Pitching Moment, Second Through Fifth Harmonic, $\mu=193$, $\psi=0$. deg.

a realistic sense, where the simulated bending-torsion moments perturbed at only 8 radial locations. The sensor location points were equally spaced at $.1R$ intervals from $r=.2R$ to $r=.9R$ where it is noted that these points coincided with specific calculation points on the blade. In this analysis, two error cases were investigated which consisted of a $\pm 2\%$ and $\pm 5\%$ random errors, respectively. The blade displacements and external loads were identified for these two error cases and only the 5% random error case is presented, Fig. 24. and 25., due to space constraints. The second error analysis consisted of perturbing the external forces and moment at all 49 radial stations with the $\pm 2\%$ and $\pm 5\%$ random errors. This analysis was performed to consider the sensitivity of the airloads and inflow identification process to errors in the external loads. Fig. 26. presents results for the identified inflow and Fig. 27. to 29. presents results for the identified airloads calculated in the wind axes system.

It can be seen, for the error cases considered, that the identified inflow and airloads are fairly insensitive to the prescribed errors. This is due to the fact that the inflow and airloads depend primarily on the external force F_{ξ} which is rather insensitive to errors of a reasonably small

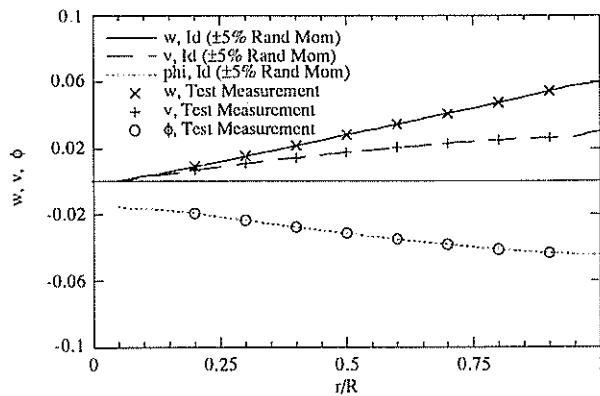


Fig. 24. $\pm 5\%$ Random Error on Moments at 8 Points, Nondimensionalized Flatwise and Chordwise Displacements and Torsion Displacement, Zeroth Harmonic, $\mu=0$.

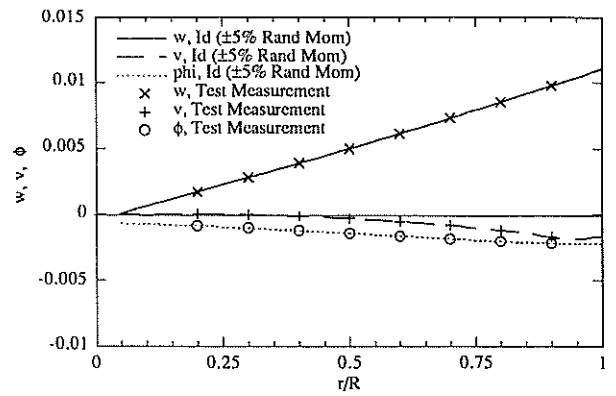


Fig. 25. $\pm 5\%$ Random Error on Moments at 8 Points, Nondimensionalized Flatwise and Chordwise Displacements and Torsion Displacement, First Harmonic, $\mu=0$, $\psi=0$.

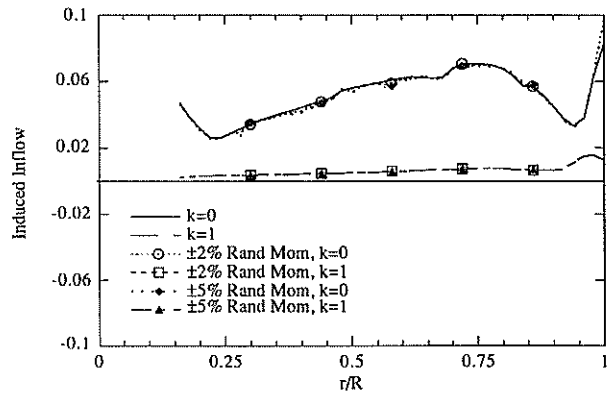


Fig. 26. $\pm 2\%$ and $\pm 5\%$ Random Errors on F_{η} and F_{ξ} Distributions, Nondimensionalized Identified Induced Flow, Zeroth and First Harmonic, $\mu=0$, $\psi=0$.

magnitude. Also, the first and higher harmonics are not greatly influenced by errors in part due to the fact that the identified displacements are insensitive to perturbations.

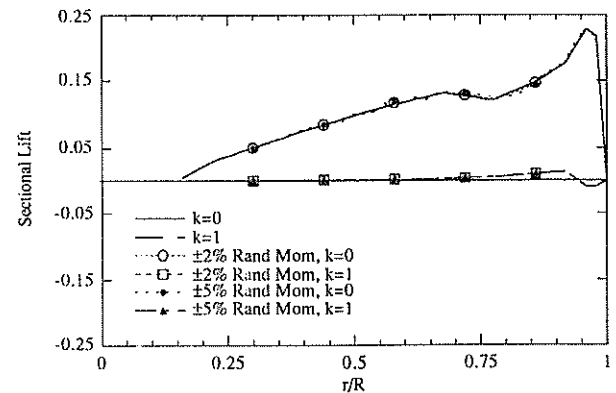


Fig. 27. $\pm 2\%$ and $\pm 5\%$ Random Errors on F_{η} and F_{ξ} Distribution, Nondimensionalized Identified Lift, Zeroth and First Harmonic, $\mu=0$, $\psi=0$. deg.

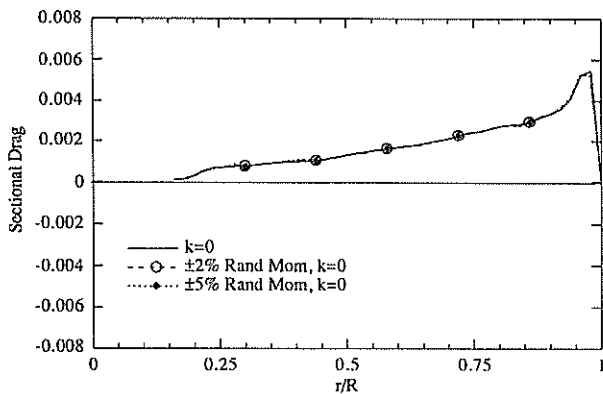


Fig. 28. $\pm 2\%$ and $\pm 5\%$ Random Errors on F_{η} and F_{ζ} Distribution, Nondimensionalized Identified Drag, Zeroth Harmonic, $\mu=0$.

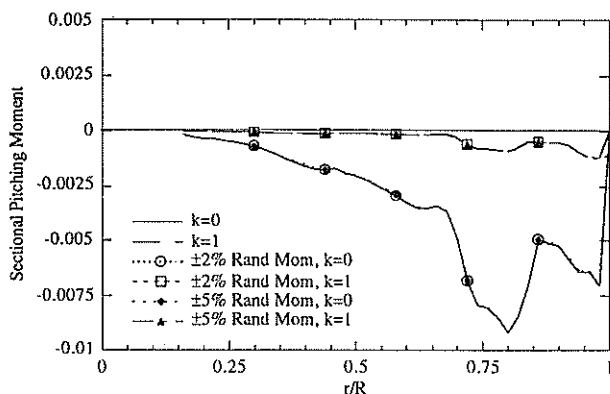


Fig. 29. $\pm 2\%$ and $\pm 5\%$ Random Errors on F_{η} and F_{ζ} Distribution, $\mu=0$, $\psi=0$. deg., Nondimensionalized Identified Aerodynamic Pitching Moment, Zeroth and First Harmonic

Conclusions

A methodology has been successfully developed which allows for the identification of the external loads, in the principal axes, acting on a fully coupled elastic flap-lag-torsion rotor blade. This method utilizes radially distributed bending and torsion moments and blade root angle information, both of which were obtained from simulated data. The approach is based on a force analysis and an extension of the transfer matrix method rather than the modal analysis method. An Eigenanalysis was employed to validate the structural dynamic equations of motion. The external blade loads identification process was validated by correlation of the results with experimental flight test data. For both the Eigenanalysis and the external blade loads identification process, the results are excellent and correlate well with the analytical and flight test data, respectively. With the external loads determined, a second methodology has been successfully developed and demonstrated which identifies the airloads in the wind axes while simultaneously identifying the required induced inflow. This second methodology is based on an iterative process and utilizes two-dimensional airfoil data, obtained from wind tunnel tests, which describes the characteristics of the airfoil section

aerodynamics. Finally, an error analysis was performed to investigate the sensitivity of the identified parameters to random errors imposed on the simulated blade moment data and external loads data. It was shown that for the parameters considered, the identification analysis was rather insensitive to the range of errors imposed and that the method is reasonably robust for airload and inflow identification.

References

- [1] Liu, S., Higman, J.P and Schrage, D.P., "Coupled Flap-Lag Rotor Blade Load Identification," Proceedings of the 51st Annual Forum of the American Helicopter Society, May 1995.
- [2] Higman, J.P. "Rotor Blade Torsional Load Identification," Kawada Technical Report, Vol. 16. January, 1997.
- [3] Houbolt, J.C. and Brooks, G.W., "Differential Equations of Motion for Combined Flapwise Bending, Chordwise Bending and Torsion of Twisted Nonuniform Rotor Blades," NACA Rep. 1346, 1958.
- [4] Isakson, G., and Easley, J.G., "Natural Frequencies in Coupled Bending and Torsion of Twisted Rotating and Nonrotating Blades," NASA CR-65, July, 1964.
- [5] Holzer, H., "The Calculation of Rotational Harmonic Motion (In German)," Berlin, Springer Verlag, 1921.
- [6] Myklestad, N.O., "A New Method of Calculating Natural Modes of Uncoupled Bending Vibration of Airplane Wings and Other Types of Beams," Journal of the Aeronautical Sciences, pp 153-162, 1944.
- [7] Mil', M.L., et al., "Helicopters: Calculation and Design, Vol. I, Aerodynamics," NASA TT F-494, September 1967, pp. 430-432.
- [8] Johnson, W., Helicopter Theory, Princeton University Press, Princeton, New Jersey, 1980.
- [9] Kufeld, R.M., Balough, D.L., Cross, J.L., Studebaker, K.F., Jennison, C.D., Bousman, W.G., "Flight Testing the UH-60A Airloads Aircraft," 50th Annual Forum Proceedings, American Helicopter Society, Washington, D.C., May, 1994.
- [10] Kufeld, R. and Bousman, W., "High Load Conditions Measured On A UH-60A In Maneuvering Flight," 51st Annual Forum Proceedings, American Helicopter Society, Fort Worth, TX, May, 1995.
- [11] Johnson, W., "A Comprehensive Analytical Model of Rotorcraft Aerodynamics and Dynamics, Johnson Aeronautics Version, Vol. I: Theory Manual, Palo Alto, CA, 1988.